Detection of Liquid Xenon Surface Waves by Light Modulation in the LUX Dark Matter Experiment

Connor Flexman

Advised by Richard Gaitskell

Brown University, Dept. of Physics,

Providence RI 02912, USA

May 6, 2016

Abstract

The Large Underground Xenon experiment is a dark matter direct detector consisting of a container of liquid xenon. Ripples in the surface of the liquid would modify the electron extraction efficiency from internal events and adversely affect the energy calibration and discrimination performance. We search for surface irregularities by pulsing an LED light above and below the xenon liquid surface and collecting the reflected and refracted photons with the built-in photomultiplier tube arrays on the top and bottom of the detector. In the datasets examined, two populations of excess signal were found with well-defined frequency ranges: one from 1-4 Hz and the other at 7-11 Hz. Over time, the calculated excess variance was over 2% of the mean in all PMTs. Efforts are ongoing to characterize the modulation of reflected and refracted signals with sufficient precision to constrain possible wave amplitudes.

I Introduction

Over the last century, evidence has mounted that most of the matter in the universe must be non-luminous. Oort's observations of the Milky Way, Zwicky's calculations of the luminosity to mass ratio of the Coma cluster, and Vera Rubin's anomalous galactic rotation curves all prompted early discussion of potential dark matter. The scientific community is presently largely convinced of a cosmological model including both dark energy and cold dark matter, or the ΛCDM cosmogony. The most up-to-date calculations suggest that only 4.8% of the universe's energy density is composed of baryonic matter, while 26% is dark matter and 69% is dark energy. Despite the accuracy of this calculation, dark matter has still never been directly detected, nor

do we know its mass or cross-section.

One of the most promising candidates for dark matter is a Weakly Interacting Massive Particle (WIMP). These particles would provide the gravitational potential needed to fit observational models, but otherwise only interact through the weak nuclear force. This explains their non-luminosity, but also implies a very small cross-section for detection.

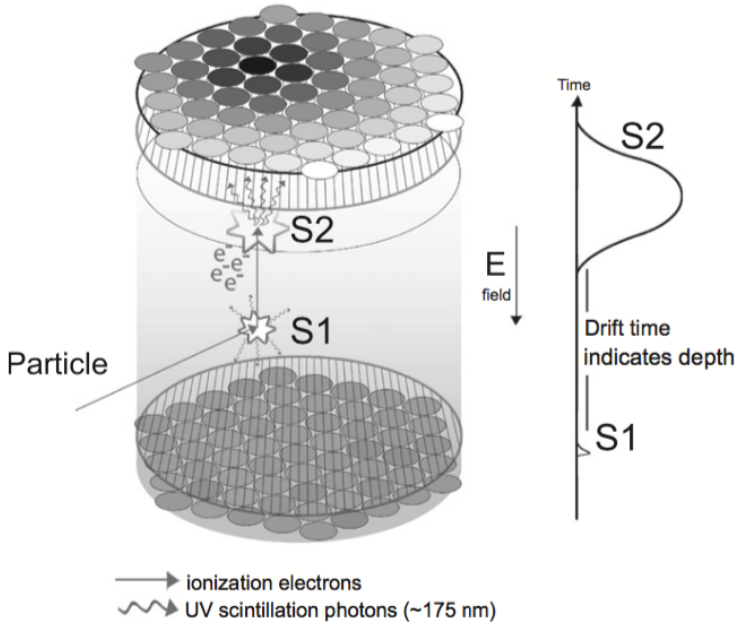

Figure 1: Reproduced from [1]. A particle interacting with the target xenon produces both an S1 and an S2 pulse. Electrons begin emitting S2 light as they are extracted from the LXe surface. Full x-y-z localization is available. The absolute sizes of S1 and S2 give information on the event's energy while the relative sizes can be used to distinguish whether the particle interacted with a xenon nucleus or orbital electron.

II The LUX Experiment

The best limits on dark matter cross-section have been set by time-projection chambers (TPCs) using targets of inert liquids such as xenon. The LUX chamber is roughly cylindrical with a 61.6 cm height and avarying width of about 55 cm, cooled to liquid xenon (LXe) temperatures at 175 K. It is filled with LXe up to 6.5 cm from the top, where a gaseous xenon stage is used. Two arrays of 3"-diameter photomultiplier tubes (PMTs) for light collection view the interior of the array on top and bottom. Interactions with xenon cause emission of scintillation light (S1) and ionization. The electrons liberated in the ionization event are drifted to the surface by means of a 180 ± 20 V cm^{-1} electric field maintained by the cathode and extraction grid within the chamber [2]. An extraction field of 6.0 kV cm^{-1} in the gas is applied by wire meshes (extraction grid

and anode grid) a half centimeter on either side of the liquid surface to send electrons into the gaseous stage where they emit electroluminescence light (S2). The hit pattern of the S2 signal localizes the x-y location of the interaction event, while the time delay between S1 and S2 is used to determine the z-location of the event by the depth of the drifted electrons.

Because of the rarity of weak interactions between dark matter and the target, special importance is placed on minimizing background. The TPC is a mile underground, such that the rock above absorbs most cosmic rays and other radiation. It is then surrounded by a water tank over 6 meters in diameter and height. This allows extensive shielding against γ-rays and neutrons from the cavern to the extent that internal radioactivity becomes the detector's largest background source. To fight internal backgrounds, the detector is made out of screened low-radioactivity materials. Xenon is also chosen as a target partly because it has no long-lived radioactive isotopes, and it is regularly purified to ensure long electron drift lengths. Further, self-shielding of the xenon is employed. Of the 370 kg of total xenon mass, the latest run used only the inner 147 kg as fiducial volume [2]. The outer xenon shields this fiducial volume from radioactivity in the materials of the detector itself.

II.1 Distinguishing Nuclear Recoils from Electron Recoils

WIMPs would interact with the detector exclusively through scattering off LXe nuclei. On the other hand, most of the detector's background is made up of β and γ radiation that scatters from LXe electrons. These electron and nuclear recoil events can be discriminated based on S2 pulse size. For a given S1 pulse size, the S2 size is statistically larger for electron recoils. Less than one percent end up in the expected nuclear recoil band. The S2/S1 ratio is therefore the primary measure allowing detection of dark matter events among background. Figure 2 shows these separated bands.

II.2 Interference of surface modulation with S2 measurements

Keeping the electron and nuclear recoil bands separated is vital to the performance and background discrimination the experiment can attain. Surface height variability is a risk to this performance due to several properties of the extraction field.

The extraction field is applied over the boundary between liquid and gas phases, but they have differing dielectric constants $\epsilon_g = 1$ in gas and $\epsilon_l = 1.874$ in liquid [3]. Then a constant voltage V_0 will produce differing fields in the gas and liquid as a function of liquid height, affecting the field-dependent extraction efficiency. We quantify this as an increase in electron extraction efficiency with surface height. An increase

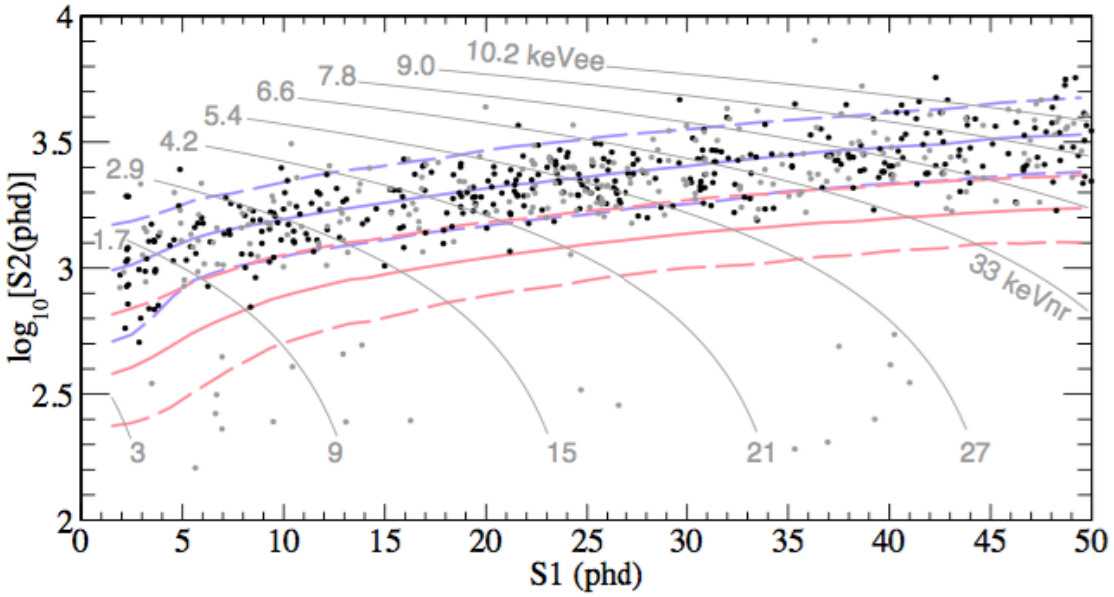

Figure 2: Reproduced from [2]. The blue lines represent the electron recoil band and the red lines the nuclear recoil band. The lines are at 50% (solid) and 10% and 90 % (dashed). The gray lines represent calibrated interaction energies. The black events have $r < 18$cm from the fiducial center and the gray events have $18 < r < 20$ cm.

in the liquid level may also reduce light emission due to shorter gas drift distance, but enhance light emission through luminescence in the stronger gas field. Quantifying these latter two effects is beyond the scope of this thesis. We can also consider the counteracting effect of an angle θ between the surface normal and the extraction field in the presence of disturbances, which we calculate after height-dependence.

We follow Griffiths [11] for discussions of polarized media. To find the field's dependence on height, we approximate the grids as a parallel plate capacitor with minimal fringing field since their separation $d = 1$ cm is much smaller than the width of 60 cm. For a liquid level height z, we can take the line integral over the electric field and reduce to

$$V_0 = \int_0^z \mathbf{E_l} \cdot d\ell + \int_z^d \mathbf{E_g} \cdot d\ell \tag{1}$$

$$= z \cdot E_l + (d - z) \cdot E_g. \tag{2}$$

We can put the liquid field in terms of the gas by considering the electric displacement $\mathbf{D}$. Gauss's law for dielectrics states that for the integral over an area that encloses free charge $\mathcal{Q}_{f_{enc}}$,

$$\oint \mathbf{D} \cdot d\mathbf{a} = \mathcal{Q}_{f_{enc}} \tag{3}$$

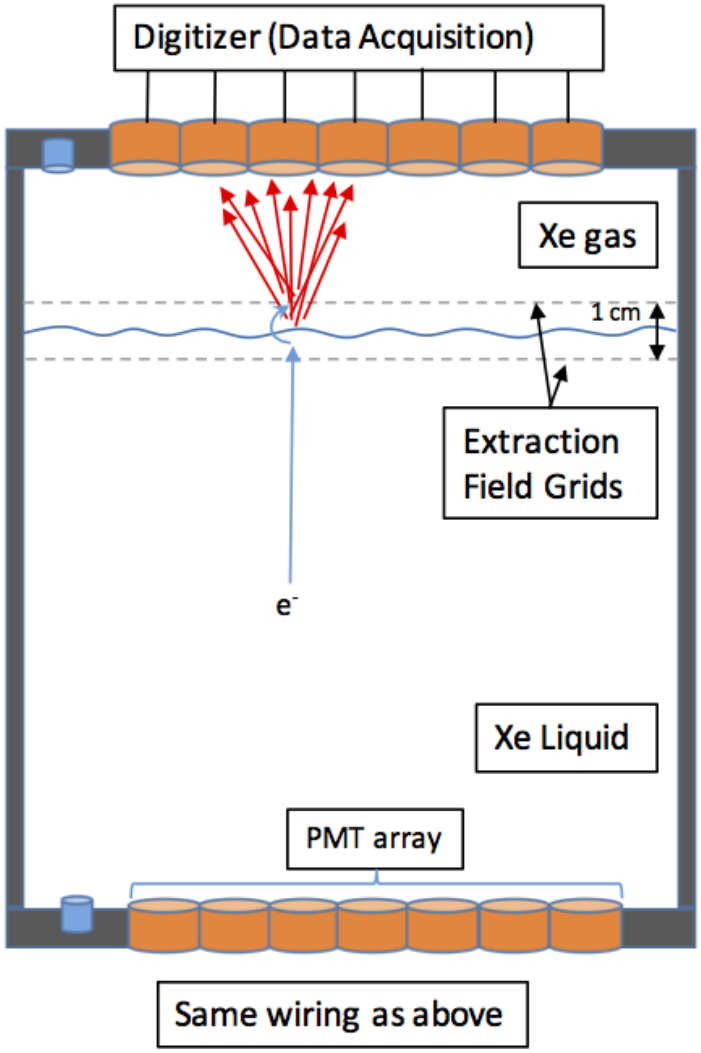

Figure 3: Rough schematic of the detector after a particle interaction. The interaction has liberated one or more electrons in the LXe, which are drifted to the surface by means of an electric field. A stronger field is applied at the surface to extract the electron into the gas phase, producing S2 scintillation light. Interference with the extraction process will lower S2 resolution and hamper the discrimination between electron and nuclear recoil.

so we can used the standard pillbox method to find $\mathbf{D}$. Substituting in a charge density σ on a parallel plate with area A, we obtain $2DA = \sigma A$ such that

$$D = \frac{\sigma}{2}. \tag{4}$$

Xenon is a linear dielectric past fields of 6 kV cm^{-1} [4]. Thus we can directly calculate the electric field $\mathbf{E}$ in a material from the displacement using

$$\mathbf{D} = \epsilon \mathbf{E}, \tag{5}$$

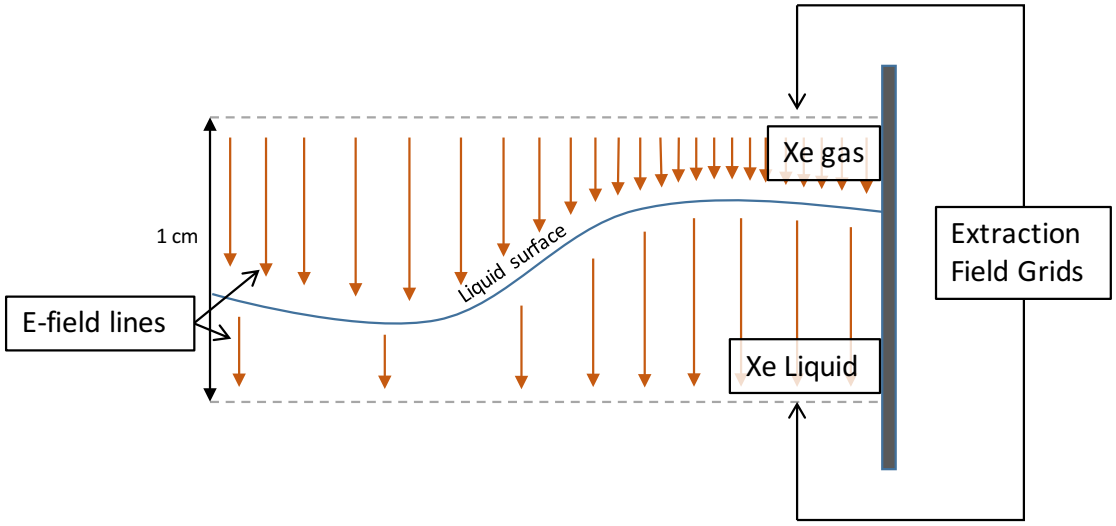

Figure 4: As the surface height increases, the extraction field for a given voltage increases significantly, increasing the electron extraction efficiency along with it. The amplitude of the expected wave is exaggerated for clarity.

where the permittivity ϵ can be replaced by the electric susceptibility via $\epsilon = \epsilon_0(1 + \chi_e)$ or the dielectric constant via $\epsilon_r = \frac{\epsilon}{\epsilon_0}$. This calculation was done using a free charge density σ on one plate, but this is equivalent to fixing σ to give some potential V_0 on that plate. Since $D = \frac{\sigma}{2}$ holds no matter the material, it must be equal in liquid and gas, such that we find

$$\epsilon_g E_g = \epsilon_l E_l. \tag{6}$$

Equation 2 then becomes

$$V_0 = z \cdot \frac{\epsilon_g}{\epsilon_l} E_g + (d - z) \cdot E_g. \tag{7}$$

Experimentally, the permittivities of xenon are $\epsilon_g \approx \epsilon_0$ and $\epsilon_l = 1.87\epsilon_0$, so let the relative permittivity $\epsilon_r \equiv 1.87$. Then we obtain the z-dependence of E by

$$E_g = \frac{V_0}{d - (1 - \frac{1}{\epsilon_r})z}. \tag{8}$$

The most recent run in LUX set $V_0 = 4.6$ kV, $d = 1$ cm and $z = 0.5$ cm at equilibrium. This allows us to calculate values of $E_g = 6.0$ kV cm^{-1} and $E_l = 3.1$ kV cm^{-1}, the same as found by [2]. We now switch to E_l to more easily compare to extraction efficiency, but this is always simply proportional to E_g. Consider small perturbations dz measured in cm from the position equidistant between the grids (note the d is an

infinitesimal, not the distance d used before). We can expand in a Taylor series and find the linear term

$$E_l \approx 6 \text{ kV cm}^{-1} + 2.1 \text{ kV cm}^{-2} \cdot dx \tag{9}$$

while Fig. 5 shows its behavior over all liquid levels.

The electron extraction efficiency is as a function of electric field is measured by [5], and [6] gives examples of modern LXe detector calibrations. The extraction efficiency during Run03 of the LUX detector measured 0.49 for a liquid field of 3.1 kV cm^{-1}. The logistic nature of the curve leaves it fairly linear around extraction efficiencies from .3 to .7, so we can estimate the field-dependence from this domain. Each plot shows slopes between .25 and .35 for these values, so take $m = 0.3 \pm 0.05$. This approximation gives an electron extraction efficiency $X \approx 0.49 + 0.3(\pm 0.05) \cdot \mathrm{d}E_l$ for small deviations $\mathrm{d}E_l$ of the liquid field. Our direct approximation for fractional change in extraction efficiency from surface height deviation becomes

$$\frac{1}{X}\frac{\partial X}{\partial z} \approx 0.12(\text{mm})^{-1}. \tag{10}$$

In comparison, an angle θ between the surface normal and the extraction field introduces a factor of $\cos\theta$ to the extraction efficiency. This angle depends on both height and wavelength, with

$$\theta = \tan^{-1}\frac{2dx}{\lambda} \tag{11}$$

$$1 - \cos\theta \approx \theta^2 \approx \left(\frac{2dx}{\lambda}\right)^2 \tag{12}$$

such that it achieves a 0.01 fractional change in extraction efficiency whenever the ratio of amplitude to wavelength is greater than 1/20. For a wave amplitude of 100μm as listed above, this would correspond to wavelengths under 2 mm.

II.3 Chamber Mechanics and Surface Disruption Processes

There are no expected causes of surface height modulation in the detector, but some possibilities. The LXe surface could be affected either through wave processes or bubbling processes. There have been four possibilities considered to date: waves might be generated from surface flow of the weir or driven by capacitive level sensors, while bubbles might be trapped in the re-condensed LXe after purification or produced by heat load of the PMT bases within the chamber. So far, heat load has been definitively ruled out and some evidence has been produced against interaction with capacitive sensors.

The LXe must be regularly cycled through a purifier to remove contaminants, radioactive and otherwise.

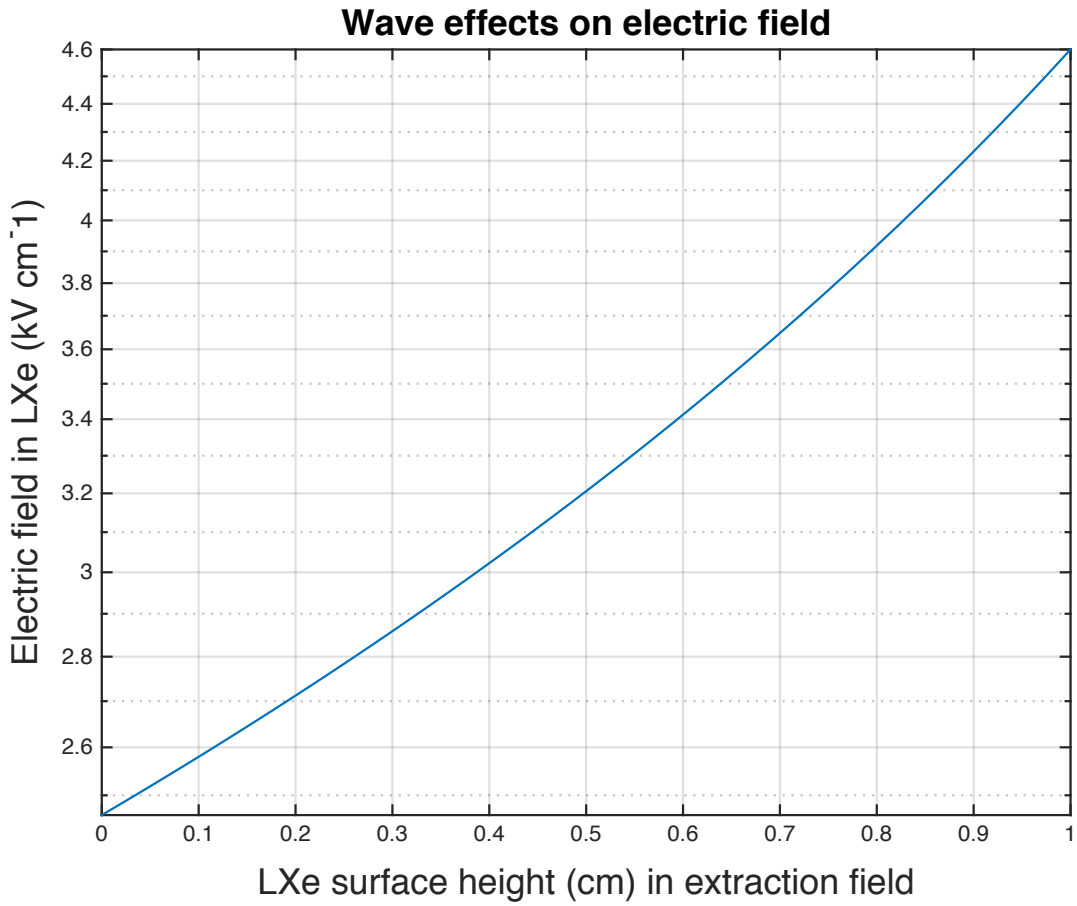

Figure 5: The response of electric field to LXe surface height is linear in small deviations. At a surface height of 0.5 cm, the field is 3.1 kV cm^{-1}.

The return rate is only 0.1 standard liter per minute (SLPM) of liquid and is injected in the bottom of the detector [1], where it should not be able to create waves, but could transport bubbles into the chamber. The xenon is purified in part by an evaporation process, and re-condenses far away from the site of re-insertion. Since xenon's surface tension is about a fourth that of water's, bubbles would more easily dissipate from a LXe surface than a water surface, meaning it is qualitatively less likely that bubbles would stay intact long enough to enter the detector by this method than intuition of water flow would imply. However, even small xenon gas bubbles that did become trapped in the re-condensed LXe would ultimately rise to the liquid surface and disturb it.

To have this dynamic purification, a weir was also added for spillover to keep the liquid level constant. This surface flow may cause submillimeter ripples around the weir's location, either as standing waves or as ephemeralities caused by changes in the flow rate. Extra variance localized near the weir could allow us to distinguish this effect. The weir's location is shown in Fig. 8.

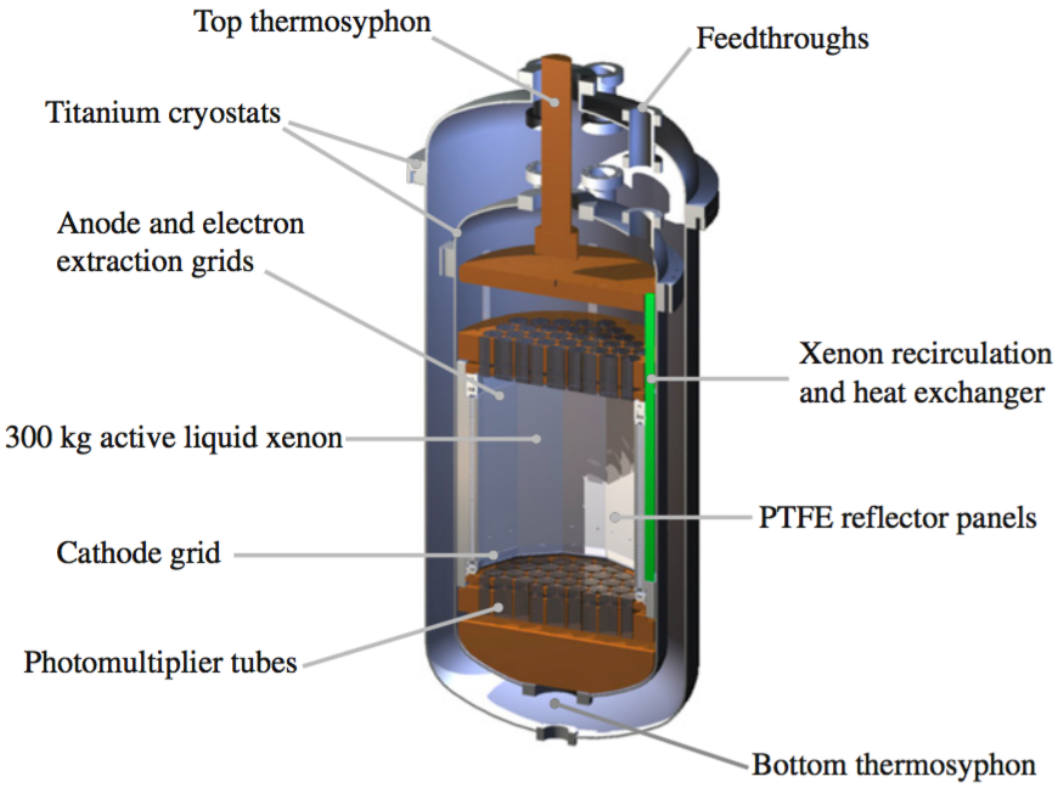

Figure 6: Reproduced from [1]. The xenon recirculation module is one possible source of surface disruption. The extraction grid around the surface produces the bound charge that could interact with the capacitative parallel-plate level sensors to drive waves.

There are also 3 level sensors around the detector at the surface. Their purpose is to monitor the LXe height. However, these parallel-plate style sensors use capacitance to measure liquid height. This leaves open the possibility that the capacitance sensors may actually drive surface modulation of their own as signal is read out and their voltage fluctuates. Free charge buildup on the LXe surface, while evident, is many orders of magnitude smaller than the surface bound charge from the extraction field discussed in Sec.III.2.3. Analysis by Jingke Xu has identified the behavior of free surface charge and the phenomenon of e-burps, delayed scintillation after S2 that could be linked to surface waves. Recent work has established that the operation of these sensors does not affect e-burps [personal communication], but does not rule out other effects yet.

III Wave Detection

III.1 Methods

The only direct apparatus for measuring the LXe surface height accurately (within $\sim 100\mu$m) in the LUX detector are the three capacitative level sensors. However, no analysis has been done on the sub-second timescales over which waves would be expected to show an effect, and there may not be reliable enough data on their baseline stability over time for this analysis to take place. If a calibration were available and these could be logged at sub-second timescales, this method should be pursued. Measuring stability of S2 width instead can give us height resolution under 200 μm [7], but timescales that can incorporate multiple S2s are too long to find surface waves. While future detectors could incorporate higher precision direct height sensors, we attempt to indirectly measure height disruption by shining LEDs in the chamber to measure changes in the refraction or reflection patterns.

The LUX chamber is equipped with 12 LEDs around its edge, with 6 on the top PMT plate and 6 on the bottom PMT plate. These are pictured in Fig. 8. The top LEDs are mounted 6.5 cm above the surface and the bottom are 55.1 cm below the surface. The LEDs are blue, with wavelengths of $\lambda = 440$ nm [2]. The LEDs each have PTFE diffusers for "more uniform" illumination [1] but no guarantee of complete isotropy. For a given dataset, a function generator powers a single LED with square pulses so that it emits bursts of light at a desired frequency. The PMT arrays on top and bottom register the photons in the detector, and a digitizer reads out the PMT anode voltages as signal. Most datasets are taken while an LED mounted on the top is activated, but some datasets use an LED on the bottom. Temporal and spatial dependence in the signal allows us to partially characterize the amplitude and frequency of the waves, so determining the characteristics of these waves will be of some use to us.

III.2 Waves in Xenon

We follow the discussion of liquid waves from Freegarde [12]. Liquid wave equations can be most easily solved by looking at limiting behavior in different regimes. When wavelengths are large compared to a characteristic surface tension length, gravity will be the primary restoring force. When wavelengths are small in comparison, intramolecular forces take over. Between the limits of these gravity waves and capillary waves, both forces must be accounted for.

The second split in regimes comes from dynamics. When wavelengths are much larger than the maximum depth, horizontal movement dominates and simplifies the equations to what we term the shallow wave regime.

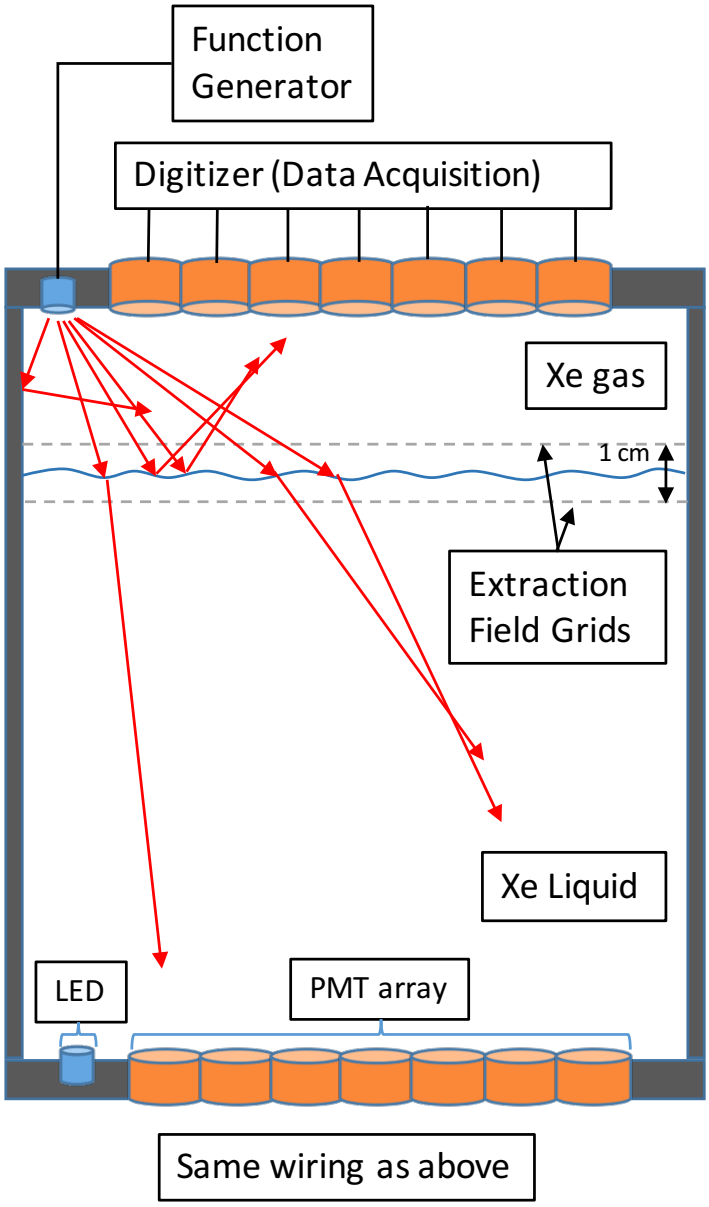

Figure 7: Rough schematic of the detector during LED function. The LED has a diffuser to increase isotropy of its output, and surface waves may direct reflected and refracted rays into focusing patterns or other temporal modulations detectable by the PMT arrays.

When depth is comparable to wavelength, vertical movement must also be taken into account for deep waves. The limit of infinite depth is also useful, but vertical movement will never dominate horizontal movement.

III.2.1 Gravity Waves

The LXe in the LUX TPC is about 65 cm deep but only 62 cm in diameter, so all wavelengths up to the maximum would be in the deep regime. Under assumptions of incompressibility and inviscid flow, the height

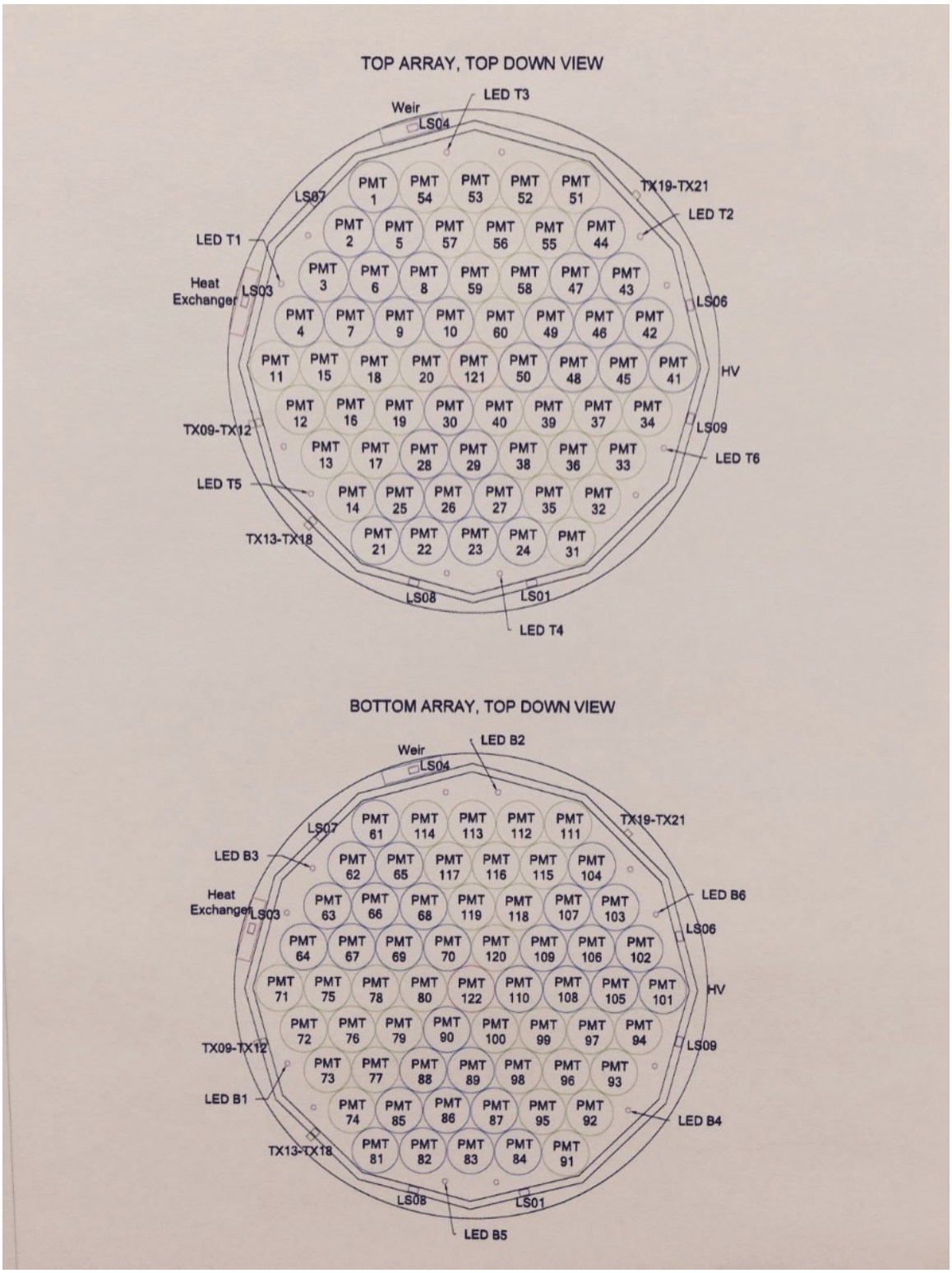

Figure 8: Both the top and the bottom of the detector are lined with a hexagonal array of PMTs for photon signal collection. The PMTs are regularly calibrated in situ to ensure good health and high sensitivity.

h of deep liquid waves obeys the equation

$$??\frac{\partial^2 h}{\partial t^2} = \frac{g\tanh(kh_0)}{k}\frac{\partial^2 h}{\partial x^2} \tag{13}$$

where g is the acceleration due to gravity, k is the wave number, and h_0 is the average height of the liquid. For a sinusoidal solution

$$h(x,t) = \cos(kx - \omega t) \tag{14}$$

where ω is the angular frequency of the wave, the differential equation tells us that

$$\omega = \sqrt{gk\tanh(kh_0)}. \tag{15}$$

Since a traveling wave will cycle once every time it moves by one wavelength λ, its frequency $f = 2\pi\omega$ can be related to its velocity v by

$$f = v/\lambda. \tag{16}$$

Multiplying both sides by 2π and rearranging, we have derived the dispersion relationship

$$v_p = \frac{\omega}{k} \tag{17}$$

where v_p is the phase velocity and equivalent to v for a monochromatic wave. Combining this relationship with Eq.15 for ω, we find that a deep liquid wave travels with phase velocity

$$v_p = \sqrt{\frac{g}{k}\tanh(kh_0)}. \tag{18}$$

For small wavelengths, kh_0 goes to infinity and $\tanh(kh_0) \approx 1$. Indeed, even for our largest possible wavelength $\lambda = 0.62$,

$$\tanh\left(\frac{2\pi}{0.62}\cdot 0.66\right) \approx 1.0000 \tag{19}$$

so we can use the approximations

$$v_p = \sqrt{\frac{g}{k}} \tag{20}$$

$$\omega = \sqrt{gk} \tag{21}$$

across our entire range of wavelengths. With these approximations, we can also calculate the group velocity of wave packets from the definition

$$v_g = \frac{d\omega}{dk} \tag{22}$$

$$= \frac{1}{2}\sqrt{\frac{g}{k}} \tag{23}$$

$$= \frac{1}{2}v_p. \tag{24}$$

III.2.2 Capillary Waves

Displacement in deep waves falls off exponentially with depth, so small enough wavelengths will engage only arbitrarily shallow amounts of liquid at the surface. At these scales, a liquid's intermolecular forces can play a large or dominating role as a restoring force. Xenon has full molecular shells and thus very small interatomic forces, but it also has high enough density in liquid form for its surface tension to play a role.

Capillary waves will have small enough wavelengths that the deep-water limit $h_0 \gg \lambda$ can be applied without qualms. Even in this limit, the full Navier-Stokes equations are lengthy to solve, but we sketch a derivation below. An incompressible section of water with vertical displacement ζ, density ρ, and surface tension σ will ultimately feel an intermolecular restoring force

$$\frac{\partial^2\zeta}{\partial t^2} = \frac{\sigma k}{\rho}\frac{\partial^2\zeta}{\partial x^2}. \tag{25}$$

Noticing that the displacement at the uppermost surface layer must change with the total height allows us to set the condition

$$\frac{\partial h}{\partial t} = \frac{\partial \zeta}{\partial t}. \tag{26}$$

Then adding the gravitational restoring force from the last section gives us

$$\frac{\partial^2\zeta}{\partial t^2} = \left(\frac{g}{k} + \frac{\sigma k}{\rho}\right)\frac{\partial^2\zeta}{\partial x^2} \tag{27}$$

where we have left off the R.H.S. factor of $\tanh(kh_0)$ by the deep-limit approximation. Analogously to the gravitational limit, we can take the capillary limit when the intermolecular term dominates the gravity term, reached as

$$k \gg \sqrt{\frac{g\rho}{\sigma}}, \tag{28}$$

and giving rise to capillary waves with

$$\omega = \sqrt{\frac{\sigma k^{3/2}}{\rho}} \tag{29}$$

$$v_p = \sqrt{\frac{\sigma k}{\rho}} \tag{30}$$

$$v_g = \frac{3}{2}\sqrt{\frac{\sigma k}{\rho}}. \tag{31}$$

When the intermolecular and gravitational terms are comparable, we include both force terms in the differential equation. Solving in the same way as Eq.**??**, the sinusoidal wave solution in full generality has

$$\omega = \sqrt{gk + \frac{\sigma k^3}{\rho}} \tag{32}$$

$$v_p = \sqrt{\frac{g}{k} + \frac{\sigma k}{\rho}} \tag{33}$$

$$v_g = \frac{g + \frac{3\sigma k^2}{\rho}}{2\sqrt{gk + \frac{\sigma k^3}{\rho}}}. \tag{34}$$

This full dispersion relation allows us to fully characterize the velocity and frequency of deep xenon waves at any wavelength.

III.2.3 Change in Wave Properties Due to Electric Field

In Sec. III.2.1 and III.2.2 above, we have used the parameters g and σ to represent the acceleration on the liquid from gravity and interatomic forces, respectively. Both of these parameters will be effectively changed in the presence of an electric field. The extraction field we apply in the negative z-direction will produce a bound charge on the LXe surface due to its polarization. This charge has both an attractive effect in the positive z-direction toward the applied voltage and a repulsive effect on neighboring atoms. These reduce the effectiveness of g and σ, respectively, and thus decrease wave velocity and frequency over the entirety of the wavelength domain. We make no calculation of this effect here, but advise it in future work.

III.3 Reflectivity

Reflectivity is governed by the Fresnel equations, derived from the boundary conditions of amplitude and phase on light transmission from one refractive index to another. Reflectivity is calculated in the limit of infinite thickness and semi-infinite boundary length, but our LXe is many orders of magnitude deeper and wider than the wavelength of LED light so reflectivity will accurately model the true reflectance.

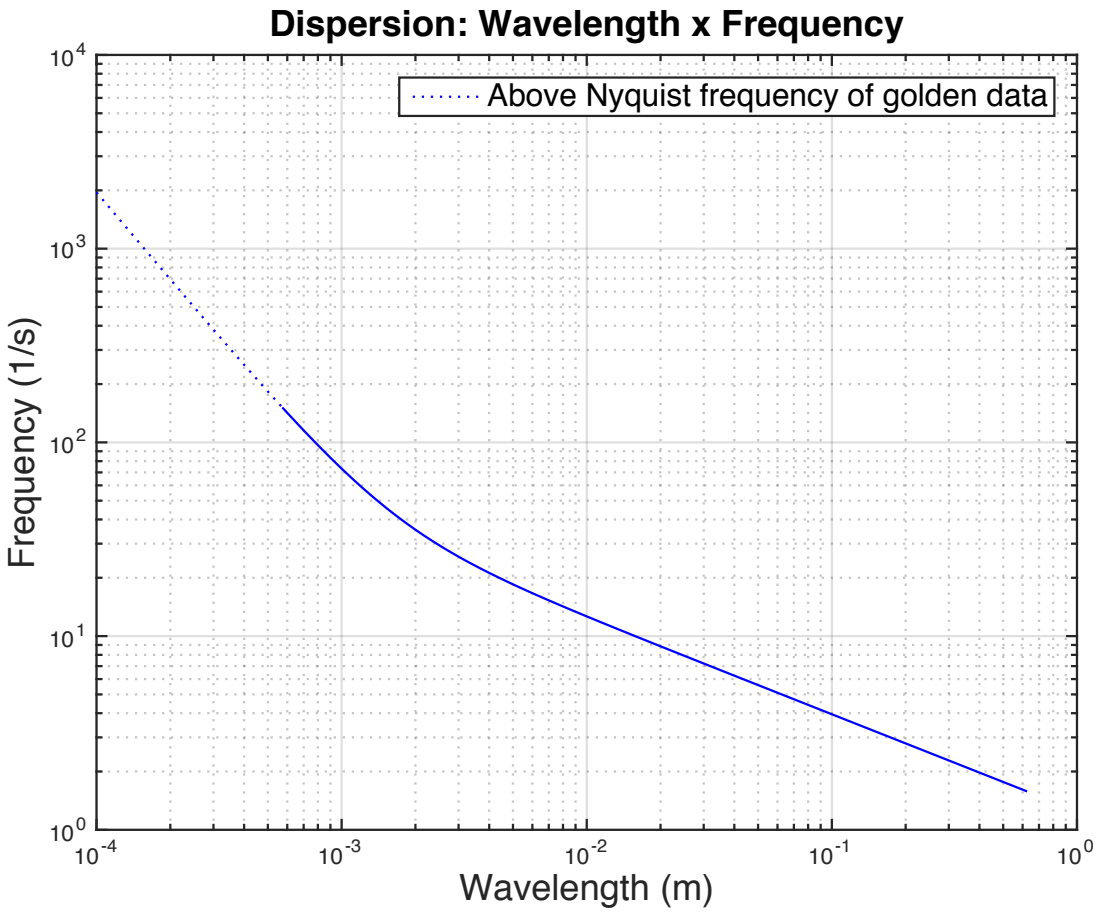

Figure 9: The one-to-one dispersion relation for LXe allows us to characterize a given signal frequency by its corresponding wavelength. The values of g and σ used assume no electric field. Our golden dataset `lux10_20151217T0930` is taken at 300 Hz, so the Nyquist frequency of 150 Hz limits our ability to see wavelengths under 6 mm for this data. This can be corrected, as other datasets have been taken at higher frequency and the capacity is limited only by the data acquisition resolution of 10^8 Hz. Note that the frequency ranges of 1-4 Hz and 7-11 Hz correspond to wavelengths of 10-60 cm and 1.5-5 cm, respectively.

The Fresnel equations differ for light polarized perpendicular to the plane of incidence (s-polarized) and parallel to it (p-polarized). For unpolarized light like is emitted by the LUX internal LEDs, the total reflectance R is given simply by the average of the reflectance of each type:

$$R = \frac{R_s + R_p}{2}. \tag{35}$$

For a non-magnetic material such as xenon, the reflectance for s-polarized light R_s is

$$R_s = \left| \frac{n_1 \cos\theta_i - n_2 \cos\theta_t}{n_1 \cos\theta_i + n_2 \cos\theta_t} \right|^2 \tag{36}$$

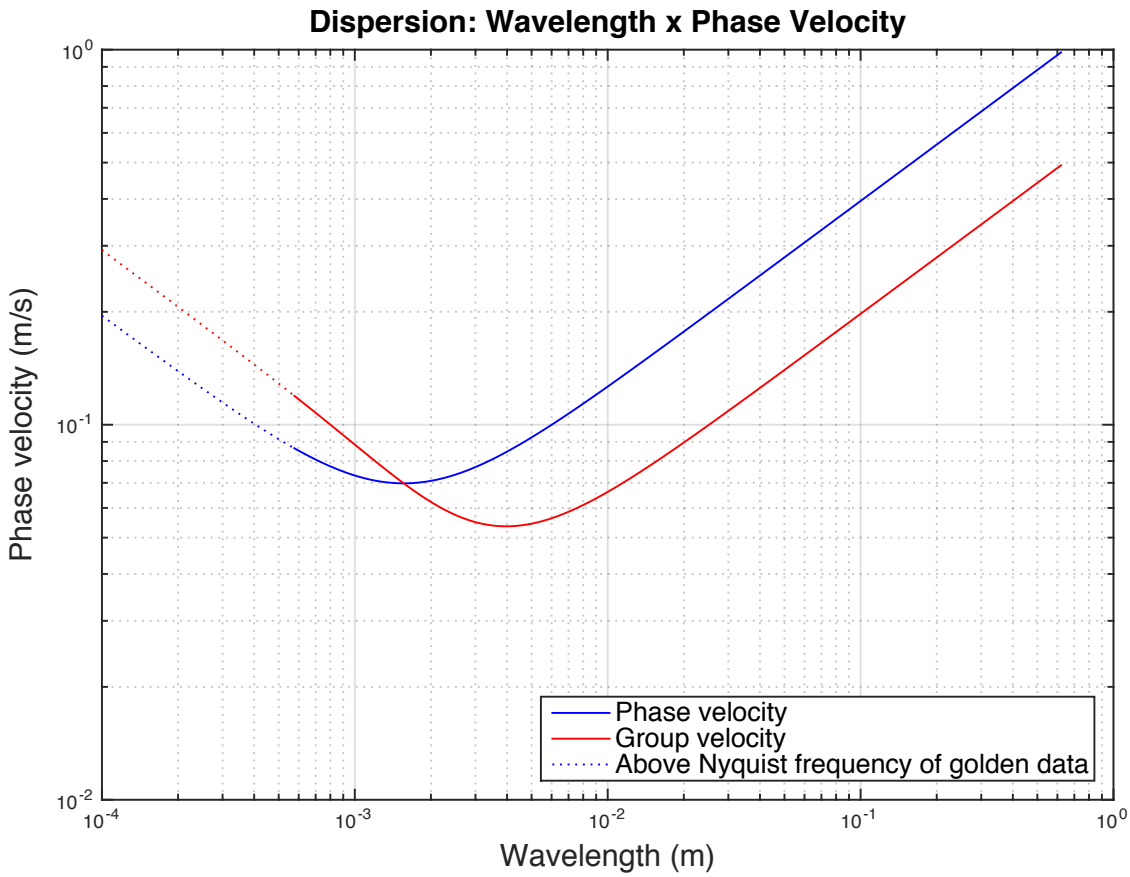

Figure 10: Surface tension drives capillary waves at low wavelengths where gravity leaves off, creating a V-shaped velocity curve. The velocities included are specific to xenon with no electric field.

whereas p-polarized light has

$$R_p = \left| \frac{n_1 \cos\theta_t - n_2 \cos\theta_i}{n_1 \cos\theta_t + n_2 \cos\theta_i} \right|^2 . \tag{37}$$

θ_i is the angle of incidence (as deviation from the surface normal), θ_t is the angle of transmission, and n_1 and n_2 the indices of refraction for the two materials. At the 440 nm wavelength of our LED, xenon gas has a refractive index of 1.00 and LXe has a refractive index of about 1.39 [8]. The angle of transmission can then be easily calculated from Snell's law as

$$\theta_t = \sin^{-1}\left(\frac{n_1}{n_2}\sin\theta_i\right) \tag{38}$$

to put the equations solely in terms of indices of refraction and the angle of incidence. The angle of incidence for a directly reflected photon can then be calculated by the detector geometry so that we know the probability of reflection for any specific ray.

The same technique works for light shone from a bottom LED. The top PMTs now receive signal modulated by refraction. Snell's law (Eq 38) gives us this angle as long as we flip the indices of refraction. Because the arcsine function's range goes past $\pi/2$, when $\sin(\theta_t) = 1$ there is a critical angle

$$\theta_c = \sin^{-1}(\frac{n_2}{n_1}) \tag{39}$$

such that incoming light with $\theta_i > \theta_c$ will be totally reflected. This would block portions of our detector from seeing light refracted directly from the bottom LED. The critical angle of xenon at 175K is $\theta_c = 46°$. The maximum angle from a bottom LED to liquid surface for a ray that will refract into a PMT is a few degrees less than this, so all of our light will be visible.

In graphical rendering it is computationally cheaper to use Schlick's approximation [9] for these calculations. This gives the specular reflection coefficient R as a simpler function of the angle of incidence θ:

$$R(\theta) = R_0 + (1 - R_0)(1 - \cos\theta)^5 \tag{40}$$

where R_0 is the reflection coefficient at $\theta = 0$ (normal to the surface) and can be calculated by

$$R_0 = \left(\frac{n_1 - n_2}{n_1 + n_2}\right)^2. \tag{41}$$

While this approximation works well at low and high angles, it does especially poorly at angles of incidence between about 0.5 and 1.2 radians, reaching over 20% error around 1 radian. Unfortunately, this is close to the angle range we are most interested in, as mentioned in the next section. Thus we employed this method to iterate the Monte Carlo's faster but generated all finished simulations with the Fresnel equations.

III.4 Simulations and Expectations

To obtain the most beneficial data, extensive simulations of the light's behavior were made beforehand. We use 1-, 2-, and 3-dimensional models in different cases, some of which are analytic and some statistical. Most models are of a top LED reflecting from the surface with top PMTs as target, but some are of a bottom LED refracting to the top PMTs. The top LED could also produce time-dependent signal by refracting into the bottom PMTs, but this signal is expected to not be very strong and we did not model it.

The chamber is completely surrounded by high-reflectivity PTFE or PMTs in 4π [1], with the electric field grids absorbing $\ll 10\%$ of light. They are made of stainless steel and have reflectivities of 57% at xenon scintillation wavelengths of 172 nm [10], and appears to be around 60% at 450 nm. Their open areas are

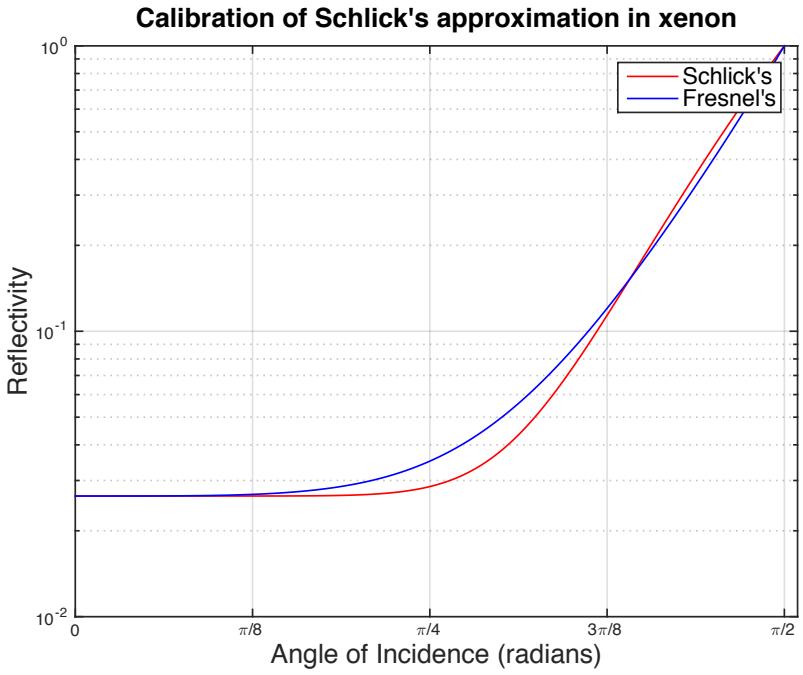

Figure 11: The Schlick approximation tracks the Fresnel equations well at low angles of incidence and in absolute terms, but deviates significantly around 1 radian.

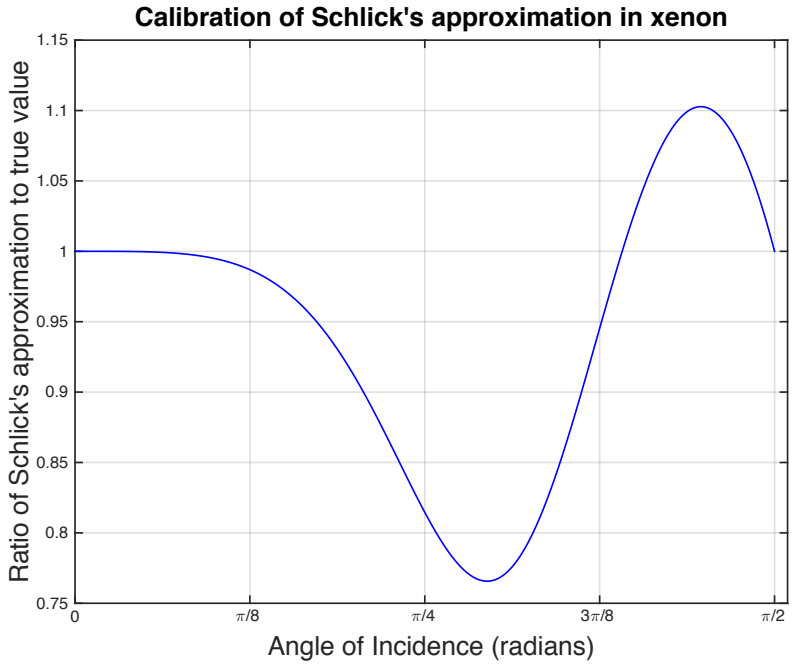

Figure 12: The ratio of Schlick's approximation to the Fresnel equations shows error of over 20% at maximum and more than 5% error over much of the range most important to us, so it could not be used for final simulations.

greater than 97%, other than the anode mesh with 88% transparency [LUX paper p28,13/14].

A Poisson process arises in situations with discrete units scattered completely independently over a state space, such that each bounded region of a given size will contain a number of units following a Poisson distribution. The number of photons emitted by an LED per unit time and the number of photons received per PMT should then both follow Poisson distributions with the relevant means. For a Poisson process with mean λ, the variance is also λ. This gives rise to the useful property that the standard deviation as a percentage of the mean is only $\sqrt{\lambda}/\lambda$, which goes to 0 as the mean is increased. To identify a dim signal, then, we want to maximize the signal to noise ratio (SNR) $\lambda/\sqrt{\lambda}$ by maximizing the mean.

Each pulse of photons in a PMT will be composed of a smaller fraction that interacted directly with the liquid surface and a larger fraction that underwent one or more non-surface interaction events, either from Rayleigh scattering in LXe, diffuse reflection from PTFE, or specular reflection from another PMT face. Even if we subtract a baseline to get rid of this diffuse background, the background will have its own Poisson variance adding to noise. Let σ be the standard deviation of a noise source. We can model the noise in a single PMT σ_{tot} as the sum in quadrature of the Poisson noise inherent to the signal and the Poisson noise of the background dependent on geometry from photons flooding the detector:

$$\sigma_{tot} = \sqrt{\sigma_{Poiss}^2 + \sigma_{background}^2} \tag{42}$$

To find a time-dependent signal from our LED, it then must stand out from the Poisson noise of both the reflected signal and all scattered radiation. Simulations show that a large fraction of both LEDs' radiation will be scattered, since not only is the quantum efficiency of the PMTs only 30% but so much of the internal solid angle is reflective PTFE. The top LED has the added difficulty that between $70-98\%$ of its radiation transmits through the surface at various angles, as shown in Fig. 13. This effect is worst nearby to the LED.

Despite the background, we can still prove that increasing the intensity in a PMT by a factor of k will monotonically increase SNR. Variance scales linearly with intensity, so if we let v_p be the variance of the Poisson noise and v_b be the variance of the background,

$$\sigma'_{tot} = \sqrt{v'_p + v'_b} = \sqrt{kv_p + kv_b} = \sqrt{k}\sqrt{v_p + v_b} = \sqrt{k} \cdot \sigma_{tot}, \text{ s.t.} \tag{43}$$

$$\text{SNR'} = \frac{\lambda'}{\sigma'_{tot}} = \frac{k\lambda}{\sqrt{k}\sigma_{tot}} = \sqrt{k} \cdot \text{SNR}. \tag{44}$$

This is the same result as above, relating an increase in mean signal to better SNR, but this time including all background noise while making no assumptions about its angular distribution or any other dependencies.

To optimize detection ability over the detector, we attempt to position the highest intensity of our LED

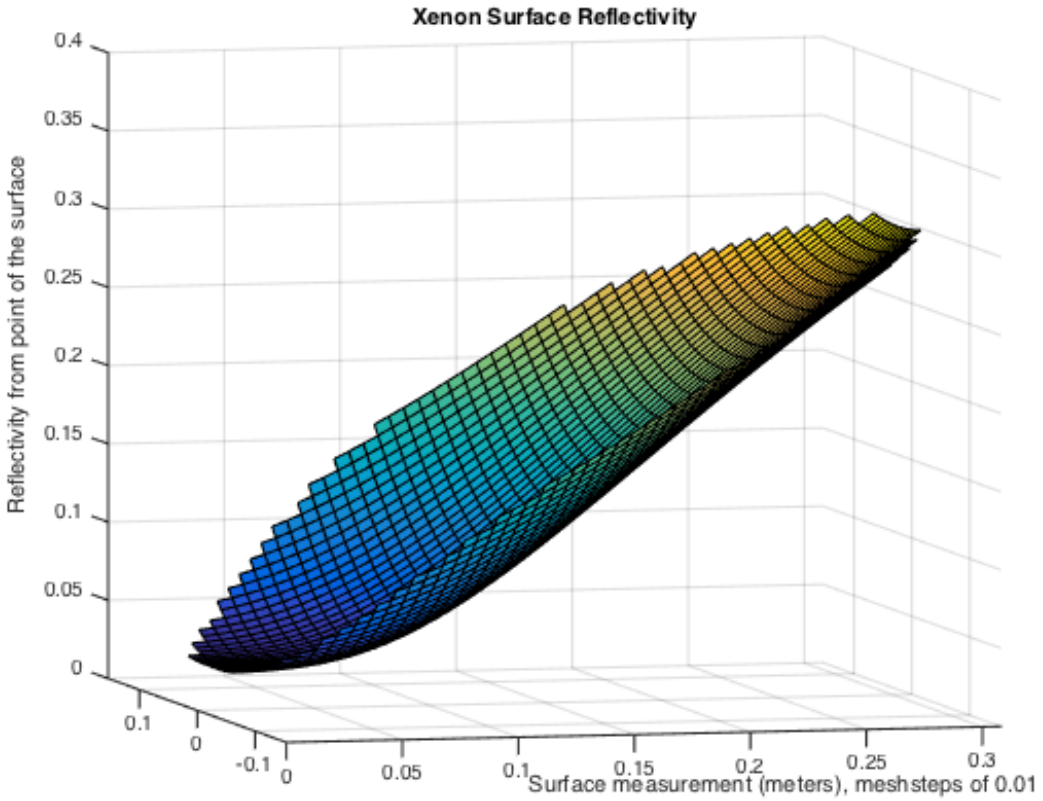

Figure 13: Using a top LED, the reflectivity of the surface goes up over an order of magnitude as angle of incidence increases further away in the detector.

(and thus highest SNR) at the point of largest time-dependence. We will call this point the target; it will be dependent on the dataset and the waves sought. We want to increase the intensity so that the target PMTs are as close to saturation as possible without reaching it. The detector's data acquisition system (DAQ) can only record up to 1900 mV in a single PMT (channel) and timestep. Any channel that saturates in a dataset must be thrown out of the analysis, because it will have artificially lower variance and mean throughout. For a specific target, we can turn the intensity up until the target is as near saturation as possible at the expense of saturating other PMTs.

A top LED will always saturate the nearest PMTs first. Let a vector $\mathbf{r}$ reach to a point the liquid surface with surface normal $\mathbf{a}$ and surface area da (which we can set to the area of a PMT face). The fractional intensity I_f reflecting from da can be given as a ratio to the total emitted intensity I_0 by

$$I_f(\mathbf{r}; da) = \frac{\Phi(\mathbf{r})da}{I_0} = \frac{R(\theta_i)\hat{\mathbf{r}} \cdot \mathbf{da}}{\int_0^{\pi}\int_0^{\pi} |\mathbf{r}|^2 \sin\theta d\theta d\phi} = \frac{R(\theta_i)\cos\theta_i da}{2\pi|\mathbf{r}|^2} \tag{45}$$

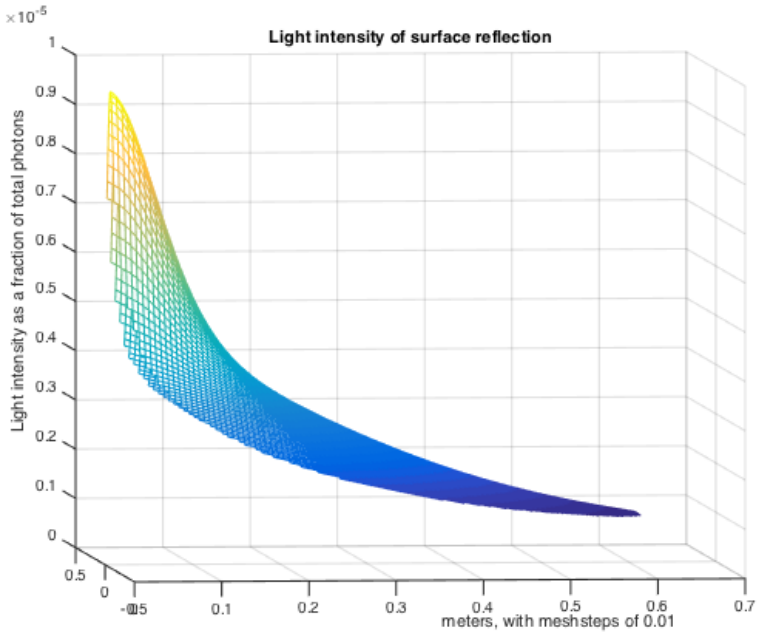

Figure 14: Althought the reflectivity increases with distance from the LED, the measured intensity falls off faster with distance. The majority of the reflected photons, and thus the expected time-dependent ones, will always be near the LED.

where R is the reflectance and θ_i the incident angle between $\mathbf{r}$ and $\mathbf{da}$. The LED can be approximated as shining in about 2π solid angle because it is mounted on the plane of the top PMT. Evaluating R, the analytical model in Fig. 14 shows that despite the order of magnitude increase in reflectivity away from the LED, the inverse r^2 and $\cos\theta_i$ dependence overpower it. Because of this, the PMTs nearest the LED will receive the greatest intensity of light. Then SNR will be highest in these PMTs and we will preferentially be able to detect waves that focus at short distances.

To determine which locations to target, we analyze a variety of surface conditions. Ray-tracing Monte Carlo simulations (MCs) like that in Fig. 16 show a strong focusing effect from rays reflected by the surface. A traveling wave across the surface should then carry small focused beams across, so that a large intensity drop in a short time would indicate the focus passing into another PMT. This would create a wave closer to square than sine. A focal point between the first and second or second and third PMT would then provide the best SNR. A wave around $A = 100\mu$m and $\lambda = 3$ cm is optimal for this focal length. Larger amplitude and longer wavelength or smaller amplitude and shorter wavelength also focus here, because larger wavelength or lower amplitude in general increases the distance of the focusing effect from the LED. Waves focused further will be harder to detect because of the lower SNR further away.

Waves of length λ will tend to have focal peaks every 2λ, so for a PMT width $w = 8$ cm the condition $2\lambda < w$ signifies that multiple peaks will start entering a PMT at once, reducing signal quality. Note also

that any top PMT signals from a reflected wave will appear to be moving twice the speed of the surface wave.

The analytical model in Fig. 15 shows how reflectivity is affected by waves. Reflectivity does change with $O(100\mu m)$ waves but will likely be a second order effect. Ray-tracing MCs showed negligible signal impact from points of high and low reflectivity. Further, it neither constructively nor destructively interferes with the focusing effect. The change in reflectivity will decrease and increase reflectance from waves with their normal pointing toward and away from the detector, respectively. The focusing effect comes from wave regions of greatest curvature, but these focusing troughs are positioned directly between the two faces of steepest gradient that influence reflectivity.

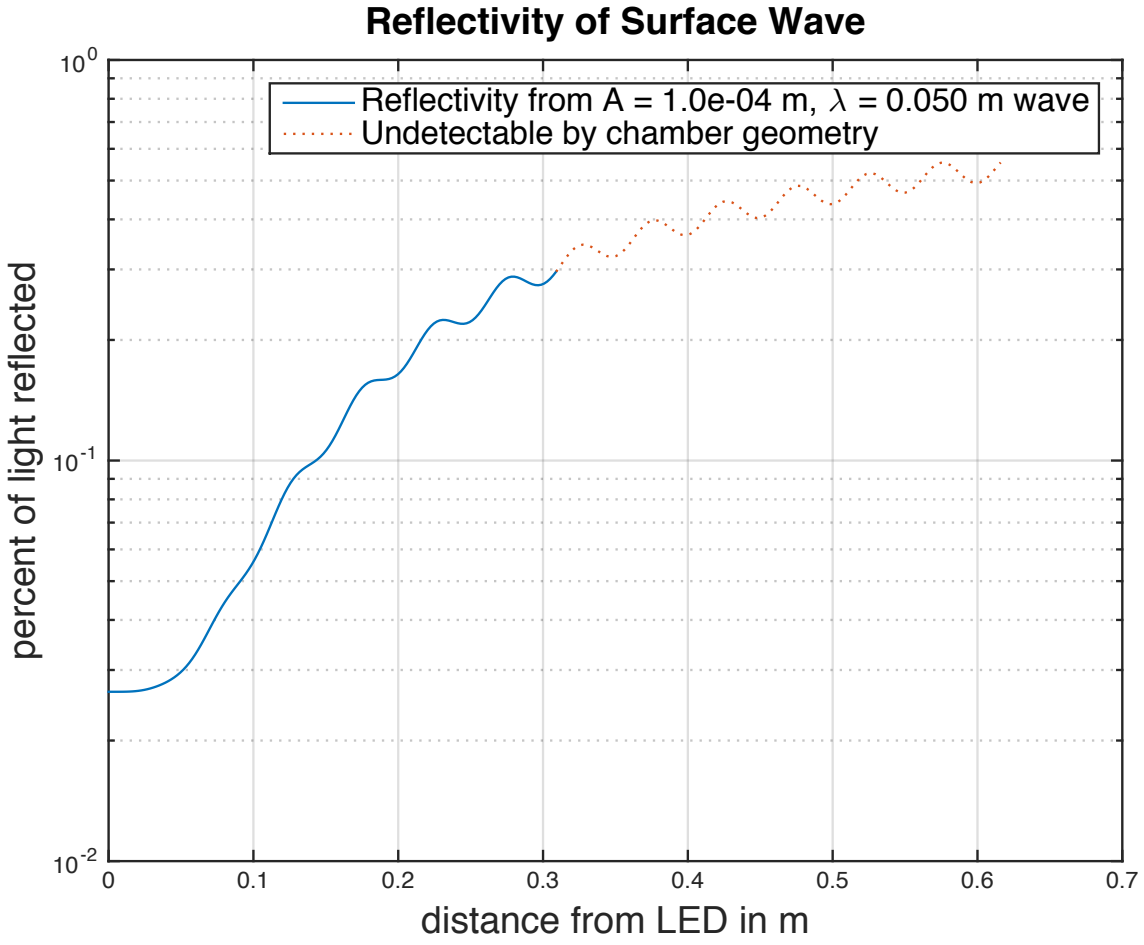

Figure 15: The reflectivity modulation (in fraction of total light, not percent as stated) from a surface wave with 100 μm amplitude and 5 cm wavelength. This will be a second-order effect compared to the focusing behavior of waves shown in Monte Carlo's. Light past about 30cm will be reflected onto the wall and not be detected after specular reflection, excluding most of the domain with large reflectivity modulation.

Time-dependent MCs allow a calculation of the expected standard deviation over time for various waves

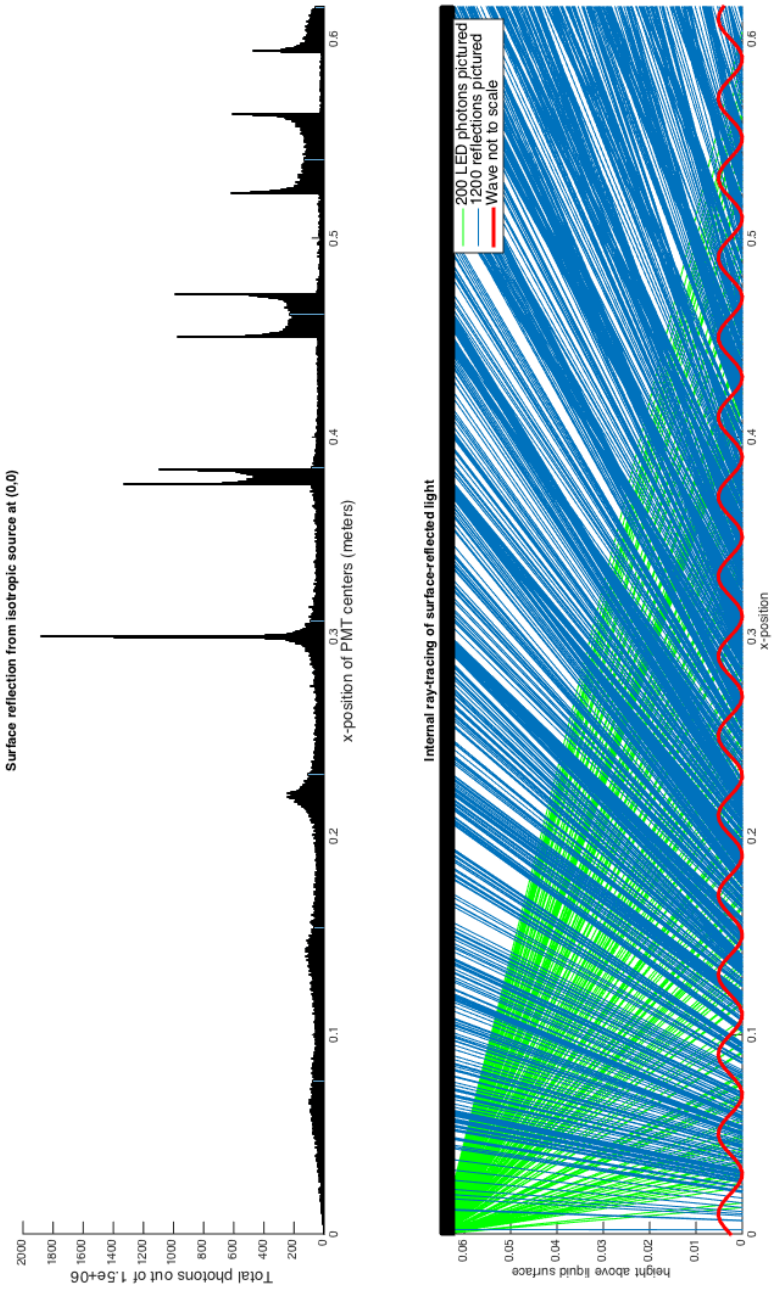

Figure 16: Monte Carlo simulation of light propagating from LED (green rays), reflecting from liquid surface (red), and being detected on the upper surface (blue). Waves on the surface with large enough amplitude and short enough frequencies tend to focus light to points. When moving from one PMT to the next, this focal point should cause abrupt changes in gathered light intensity.

as a function of distance from LED. It is also possible to extract expected PMT correlations from these simulations. Both of these projects are in progress, but hampered by poor understanding of the magnitude and distribution of the diffuse background.

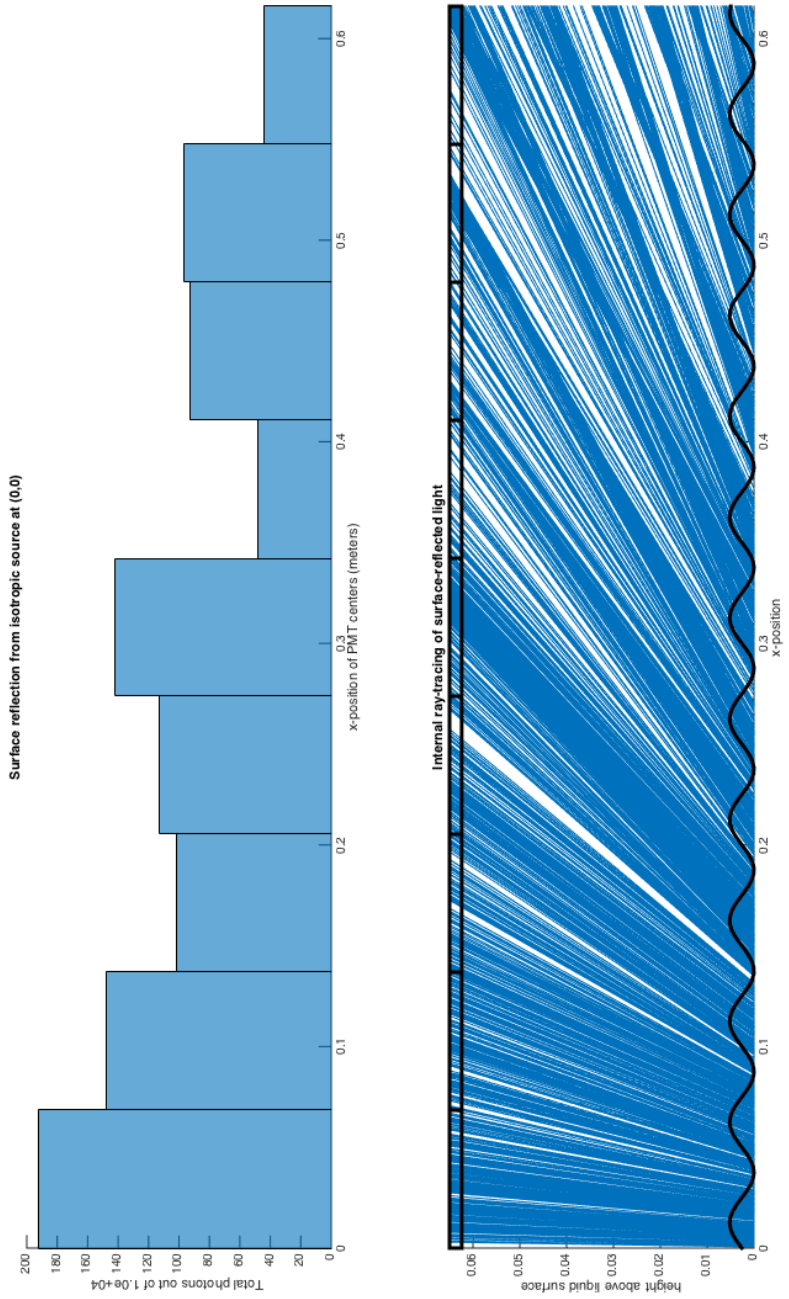

Figure 17: This simulation was done as a cross-section of the full 2D surface accounting for proper fall-off with distance and correctly-sized PMTs. An animated version can be seen at a 3x slowdown with A = 100 μm and λ = 5.3cm at <http://bit.ly/1rYGA0Z>.

However, even if the specular reflection or direct refraction cannot stand out from the Poisson background in a characterizable way, it's possible that the scattered light will still exhibit time-dependence due to the geometry. This would manifest as interfering waveforms that increase variance or show up as extra power at given locations in the frequency spectrum without being visible by eye. In section IV, we explain evidence

for this in our data.

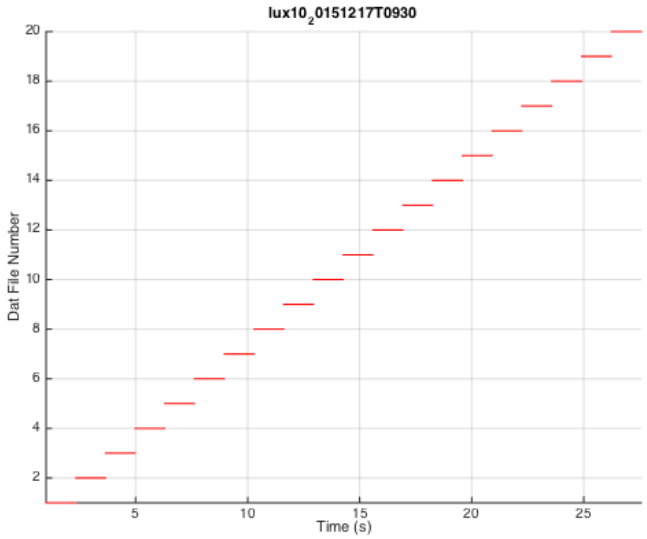

Figure 18: Our golden dataset has data buffers abutting each other, with only the ineradicable 2.5 ms deadtime between. Since we pulsed at 300 Hz, there are 3.3 ms between pulses, so the deadtime falls between the buffer-saturating pulse and the next pulse. Analysis confirms that all pulses are separated by an interval of 3.3 ms and no more.

III.5 Datasets

The LUX DAQ operates using two alternating buffers. If the buffers both fill, deadtime ensues. The frequency of interruptions for deadtime then becomes the lowest frequency detectable via Fourier transform. To avoid this constraint, data was taken at low enough intensity and frequency (300 Hz for the golden dataset) so as to not overflow the buffers, as shown in Fig. 18. Discussion of different sampling techniques for future use is in Sec. V.

All datasets show time-variation in the total LED output intensity that is far above Poisson levels. However, no time-dependence appears in the Fourier transform. To rid the datasets of this noise source, we divide each channel by the sum of all channels at every timestep to produce a normalized signal. This percentage of total signal received by each channel is the standard signal we use for all discussion of results. The normalized dataset at each timestep then follows a multinomial distribution scaled by the total intensity, which we can take advantage of for simulation.

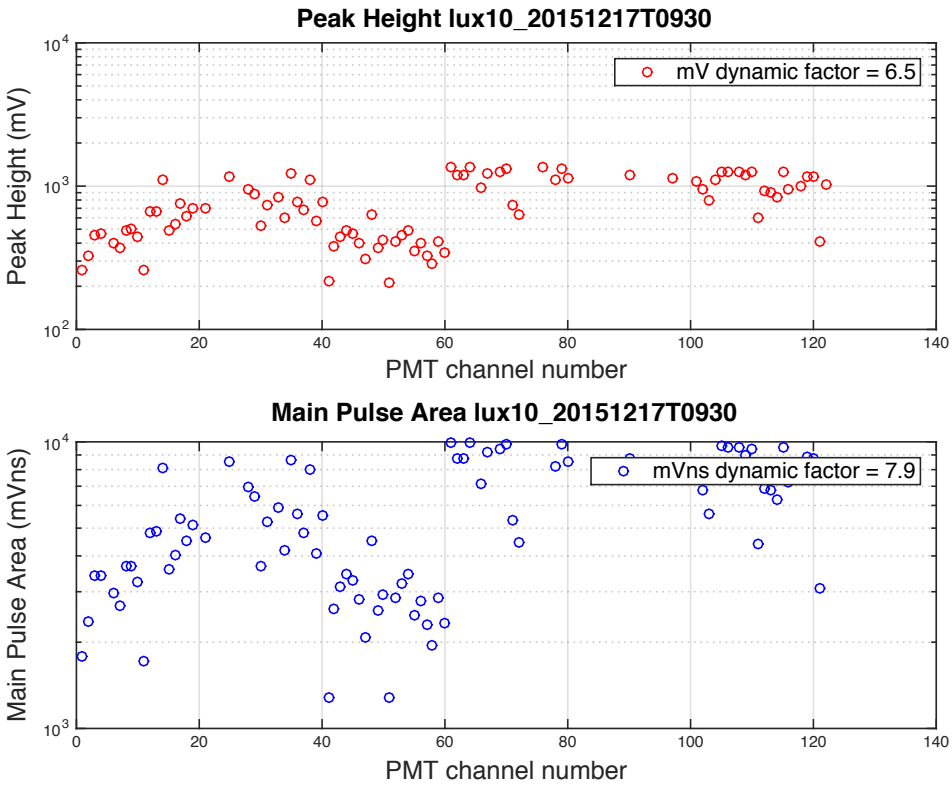

Figure 19: Pulse area does not scale linearly with pulse height, so the former should be used to characterize PMT signals. This golden dataset shows the saturation cap at 1.875 mV.

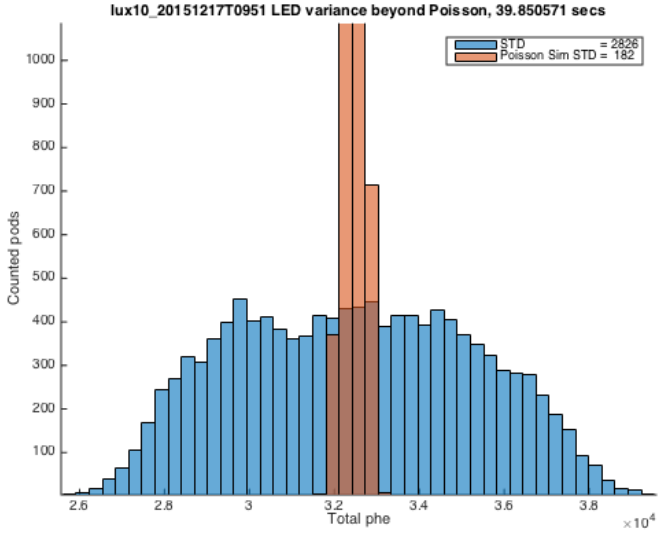

Figure 20: LED variability can be calculated using the sum of all PMT signals at each timestep. This distribution was normalized out of the individual channel data by dividing each by the sum at each timestep.

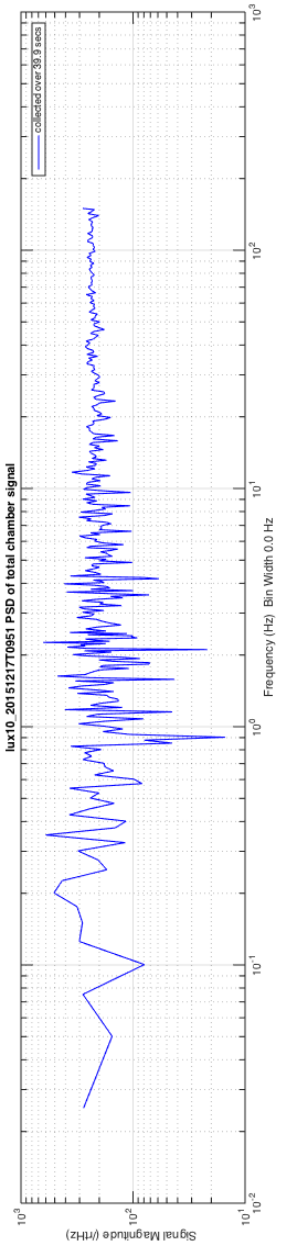

Figure 21: The LED noise has no visible characteristic frequency.

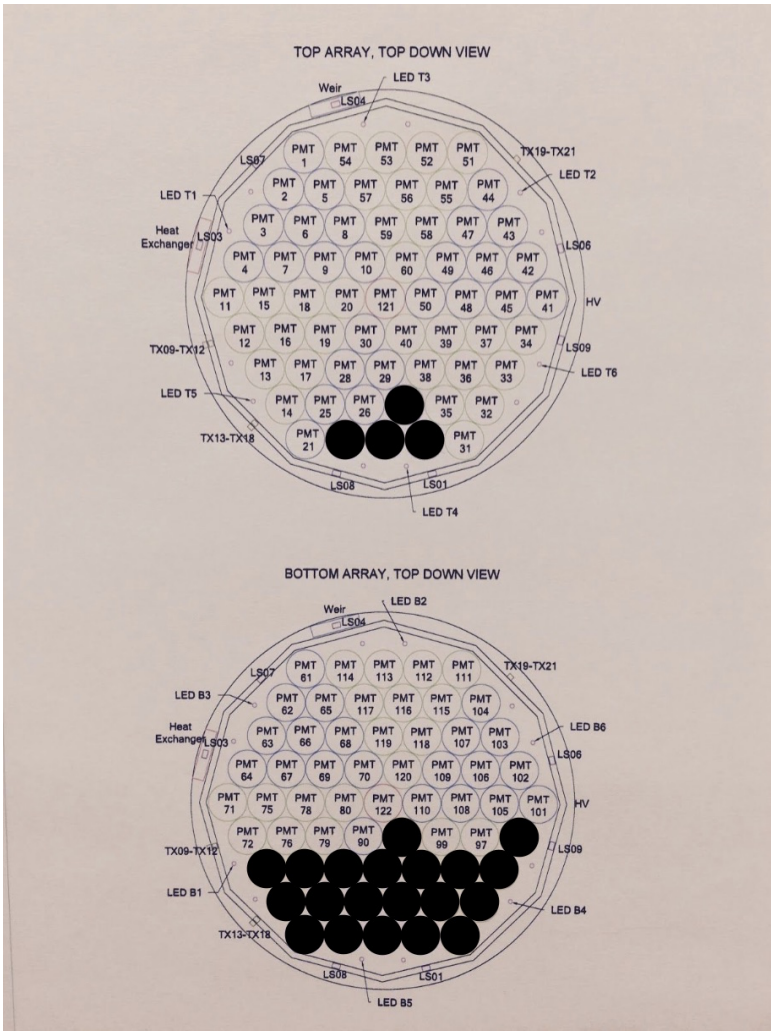

Figure 22: We pulsed LED T4 in our golden dataset. It was taken so as to saturate a few of the nearest top PMTs and many of the bottom ones (black). This maximized the signal in the 2nd and 3rd PMTs away from the LED, giving us high SNR at this border where we expect waveforms to exhibit maximum time-dependence.

IV Results

We have systematically found extra variance in gathered light intensity and two separated frequency populations with excess power.

The standard deviation found in all PMTs was above that predicted. The model used simulates PMT channels by a multinomial distribution scaled by the total intensity registered by all PMTs at a given timestep. This multinomial characterizes the nature of discrete Poisson variance. We introduce an additional term for variance of the gain in a PMT over multiple photoelectrons. If we define a standard deviation per photoelectron σ_{phe}, the total standard deviation from gain will scale as $\sigma_{gain} = \sqrt{n} \cdot \sigma_{phe}$. Then we can define the

excess standard deviation by

$$\sigma_{excess} = \sqrt{\sigma^2_{measured} - \left(\sigma^2_{Poiss} + \sigma^2_{gain}\right)} \tag{46}$$

This excess standard deviation was always positive, as shown in Fig. 23. An example histogram of the event distributions between simulation and signal is shown in Fig. 24.

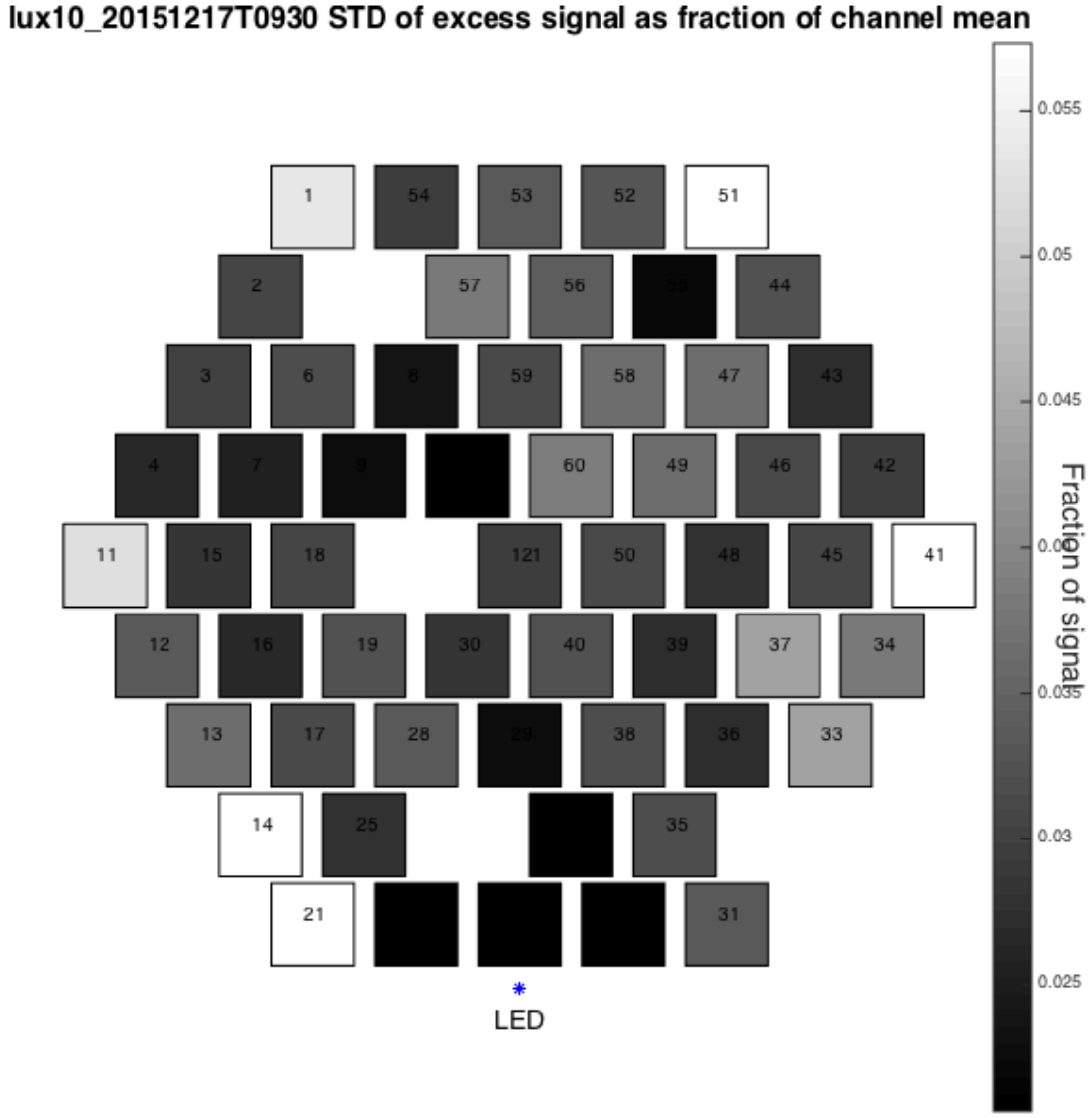

Figure 23: All PMTs show positive calculated variance in excess of prediction. The predicted values were calculated using a multinomial distribution reflecting Poisson noise and an additional term for the intrinsic standard deviation of the gain in each PMT.

Characteristic frequencies are revealed by the timeseries as well. An example signal in Fig. 26 shows strong oscillation not present in the simulation. The power spectra in Figs. **??** and 25 confirm this, with

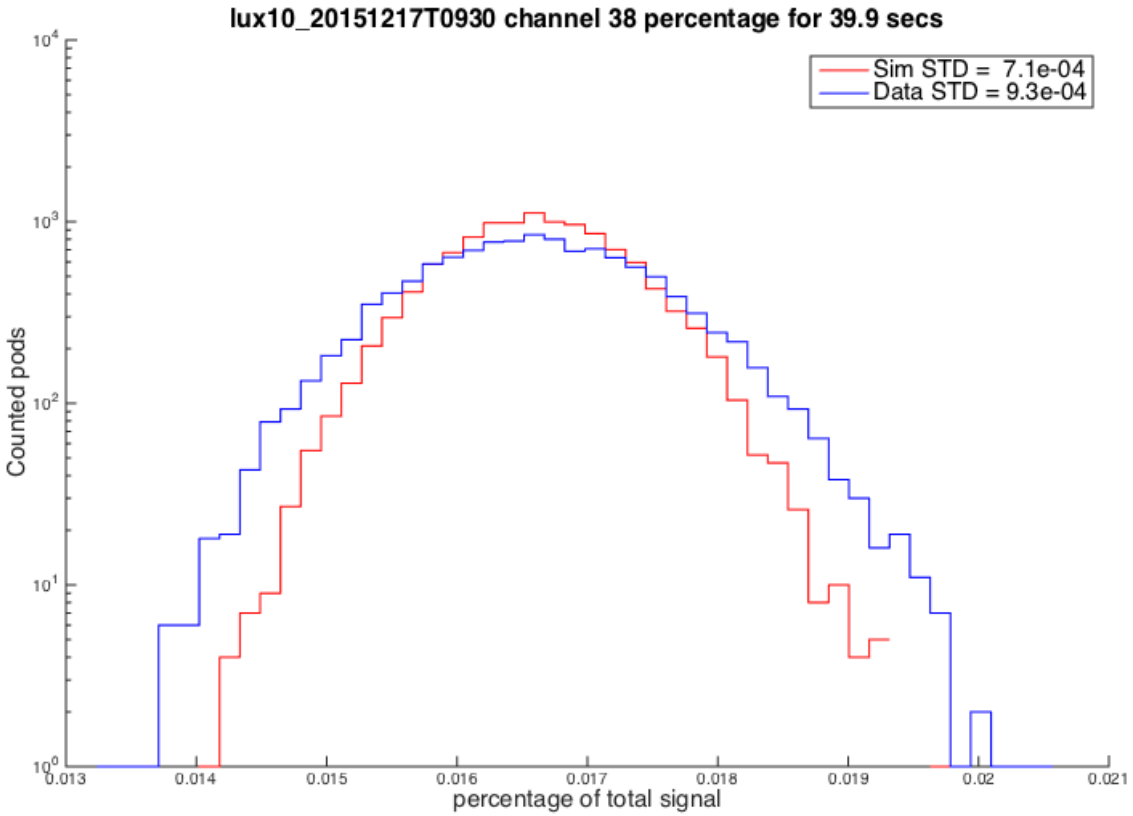

Figure 24: Histogram of simulation events and signal events in channel 38 on the detector ceiling.

excess power compared to simulation occurring at a spread from about 7-11 Hz and a potential further excess below 3 Hz. These frequencies correspond roughly to wavelengths of 1.5-5 cm and 10-60 cm, respectively.

Correlation analyses were expected to show significant signal between neighboring PMTs, but evidence of this effect was mixed. A single high-frequency wave passing over the surface would give rise to anticorrelations in the direction of movement. Instead, correlations were typically zero or positive. This effect could be produced by low-frequency waves with high focal length aiming light toward groups of PMTs rather than passing a high-resolution focal point from one PMT to the next. The study is also confounded by the fact that any time more than one wave is traveling the surface at a time, correlations would be much more complex. For multiple waves with durations on the order of seconds coming into existence and then being damped, we might expect to see the data we do: little anticorrelation, some signal over a frequency range, and general excess standard deviation. 1.5 second intervals of the dataset analyzed on their own tended to show a 7-11 Hz signal in the Fourier transform just over half the time.

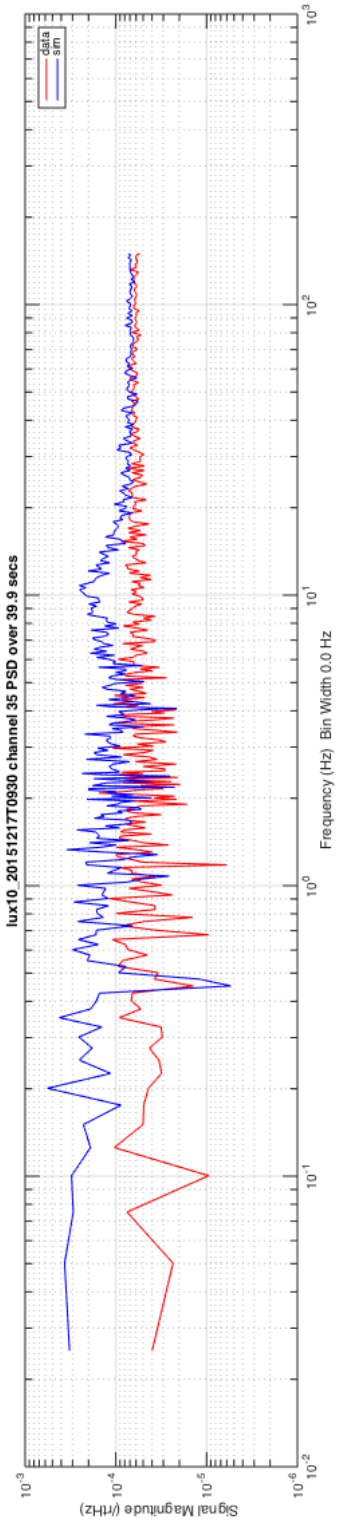

Figure 25: Power spectrum of channel 35 compared to simulation.

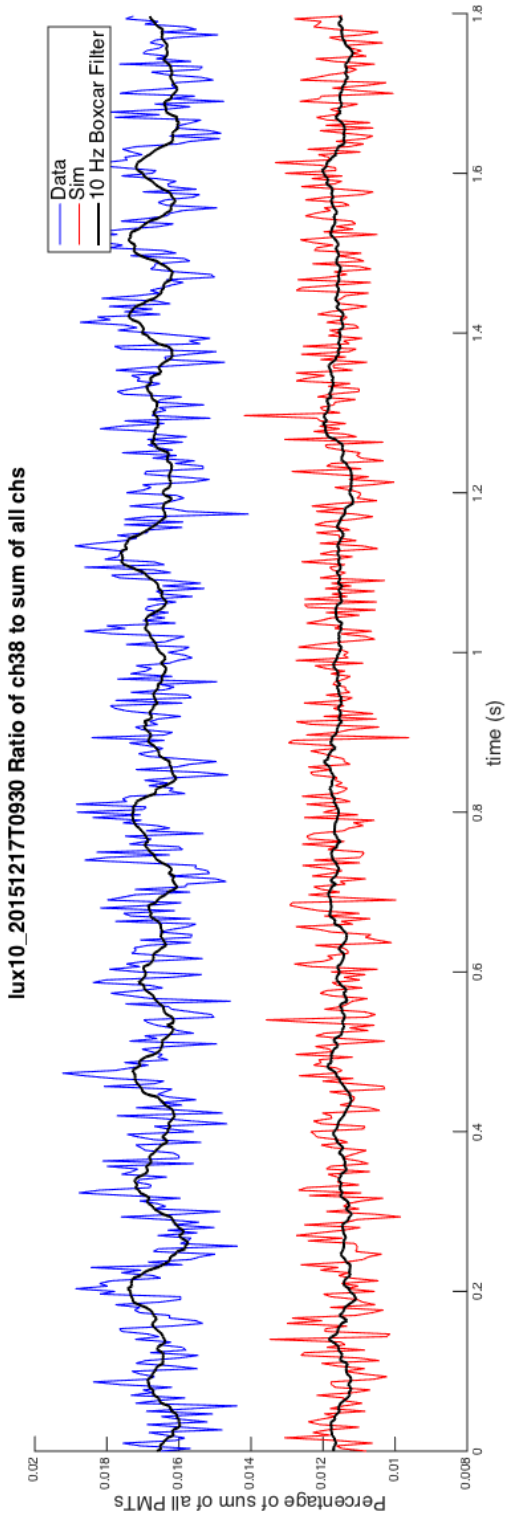

Figure 26: Signal of channel 38 using a lowpass filter at 10 Hz superposed on the original signal. The same is shown for simulated signal on the bottom.

V Conclusion

This work has found significant evidence of surface disruption on the LUX LXe surface. However, diffuse background in the detector and a variety of systematics needing correction have made it difficult to put precise bounds on the visible signal or the expected magnitude of the surface disruptions causing it. To this end, a variety of future analyses may help to clarify this issue both in LUX detector and in future two-phase particle detectors.

The limitations of our current datasets are one barrier that is easy to bypass. While some of the excess variance is explained by the 4 and 10 Hz power spectrum features, our golden dataset's 150 Hz Nyquist frequency precludes us from directly detecting any higher-frequency contributions. Waves faster than this would likely show up as excess variance directed toward the near-LED PMTs, in line with our findings. Other work by Jingke Xu has also pointed toward potential capillary waves on the order of a kHz, so this should be explored.

The difficulty with pulsing the LED at this rate is that the buffers fill up faster than they can dump the data, so there is deadtime within the dataset. For kHz modes, however, we could analyze each buffer dump separately and they would have to last only a few milliseconds for frequency analysis to be illuminating. Focusing effects would be strongly reduced in kHz surface waves, but this might be overcome by a higher general SNR obtained by faster pulsing frequency. With 5 millisecond buffer times compared to the golden dataset's 2 seconds, we could collect 400 times as much data per second. Looking for waves at 1 kHz would require 100 times more data per second than 10 Hz waves, but reduced focusing would increase this ratio. Overall, the experiments would seem of comparable order in SNR.

Instead of pulsing the LED in discrete units, we could also apply a constant voltage and take continuous data. The most reasonable analysis would be to integrate intervals over this Poisson process to generate discrete data points at some frequency, as above, but this method would help avoid pulse pileup and saturation. A better SNR could in this way be obtained, perhaps significantly if properly tuned.

There is also use for a variety of other datasets. Entirely unsaturated datasets are needed to characterize the shape of the background in the detector. Using an LED at a different position on the detector ceiling will illuminate difference between localized waves and positional effects of the LED and PMTs. Datasets are already taken during pulsing of an LED on the bottom, so one should be analyzed to ensure that this configuration does not significantly increase signal or divulge extra effects.

Other actions outside of LED data may also prove helpful. The dependence of S2 on liquid height could be strongly modified by the other affects noted in II.2, which may increase or decrease our concern about surface fluctuations. The bound charge on the liquid surface will decrease the speed of waves, so a proper character-

ization should take this into account. If evidence for surface disruptions continues to accumulate, building small models of LXe condensers and weirs to look for waves may be prudent. A higher-resolution direct height detector may also be worth considering for addition to the next generation of two-phase detectors.

References

[1] D S Akerib *et al.*, Nucl. Instrum. Meth. Phys. Res., Sect. A **704**, 111 (2013).

[2] D S Akerib *et al.*, Phys. Rev. Lett. **116**, 161301 (2016).

[3] R L Amey and R H Cole, Journ. Chem. Phys., **40**(1), 146 (1964).

[4] E Aprile *et al.*, IEEE Trans. Nucl. Sci., **51**(5), 1986 (2004).

[5] E M Gushchin *et al.*, Sov. Phys. JETP, **55**(5), 860 (1982).

[6] E Bernard *et al.*, The Design and Operation of the PIXeY Xenon Detector and a New Measurement of Electron Extraction Efficiency from a Liquid Xenon Surface, oral presentation (2015).

[7] D S Akerib *et al.*, Phys. Rev. Lett. **112**, 091303 (2014).

[8] A C Sinnock and B L Smith, Phys. Rev., **181**(3), 1297 (1969).

[9] C Schlick, Proc. Euro. 94 Comp. Graph. For., **13**(3), 233 (1994).

[10] S Bricola *et al.*, Nucl. Phys. B - Proc. Suppl., **172**, 260 (2007).

[11] D J Griffiths, Introduction to Electrodynamics (4th ed.), (2012).

[12] T Freegarde, Introduction to the Physics of Waves, (2012).